

# Solving the MHD Equations by the Space-Time Conservation Element and Solution Element Method

Moujin Zhang<sup>1</sup>, S.-T. John Yu<sup>1\*</sup>, S.-C. Henry Lin<sup>2</sup>,  
Sin-Chung Chang<sup>3</sup>, and Isaiah Blankson

<sup>1</sup>Mechanical Engineering Department, the Ohio State University, Columbus, OH 43202

<sup>2</sup>General Motor Corporation, Warren, MI 48090

<sup>3</sup>NASA Glenn Research Center, Cleveland, OH 44135

**Keywords:** MHD, the CESE method, constraint transport

\*Corresponding Author:

Professor S.-T. John Yu  
Mechanical Engineering Department  
The Ohio State University  
650 Ackerman Road, Suite #255  
Columbus, OH 43202  
Tel: 614-292-2902  
Fax: 614-292-3163

## Abstract

We apply the Space-Time Conservation Element and Solution Element (CESE) method to solve the ideal MHD equations with special emphasis on satisfying the divergence free constraint of magnetic field, i.e.,  $\nabla \cdot \mathbf{B} = 0$ . In the setting of the CESE method, four approaches are employed: (i) the original CESE method without any additional treatment, (ii) a simple corrector procedure to update the spatial derivatives of magnetic field  $\mathbf{B}$  after each time marching step to enforce  $\nabla \cdot \mathbf{B} = 0$  at all mesh nodes, (iii) an constraint-transport method by using a special staggered mesh to calculate magnetic field  $\mathbf{B}$ , and (iv) the projection method by solving a Poisson solver after each time marching step. To demonstrate the capabilities of these methods, two benchmark MHD flows are calculated (i) a rotated one-dimensional MHD shock tube problem, and (ii) a MHD vortex problem. The results show no differences between different approaches and all results compare favorably with previously reported data.

# 1 Introduction

While many Computational Fluid Dynamics (CFD) methods have been successfully developed for gas dynamics, extension of these methods for solving the Magneto-Hydro-Dynamic (MHD) equations involves unique requirements and poses greater challenges [1-14]. In particular, for multi-dimensional MHD problems, it is critical to maintain the divergence-free constraint of magnetic field, i.e.,  $\nabla \cdot \mathbf{B} = 0$ , at all locations in the space-time domain. Analytically, the constraint is ensured if it is satisfied in the initial condition. However, it has been difficult to maintain this constraint in calculating evolving MHD problems. Violating the constraint allows numerical errors to be accumulated over the computational time, leading to erroneous solutions and/or numerical instability.

To satisfy  $\nabla \cdot \mathbf{B} = 0$ , a special treatment directly incorporated into the CFD method employed is often required. Special treatments have been categorized into three groups: (i) The projection method, e.g., Brackbill and Barnes [5]: At each time step, the method solves a Poisson equation to update the magnetic field to enforce  $\nabla \cdot \mathbf{B} = 0$ . (ii) The eight-wave formulation by Powell [6]:  $\nabla \cdot \mathbf{B}$  is not treated as zero in deriving the MHD equations, leading to additional source/sink terms in equations for  $\mathbf{B}$ . The CFD solver employed would activate the sink/source terms to counter the unbalanced  $\nabla \cdot \mathbf{B}$  in numerical solutions. (iii) The constrained-transport procedure, e.g., Evans and Hawley [7], Dai and Woodward [8], Balsara and Spice [9], and Toth [12], based on the use of staggered mesh to enforce the constraint at certain spots of the control volume. Various versions of these three approaches have been developed to solve the MHD equations in multiple spatial dimensions [4-13]. Recently, these methods have been assessed and summarized by Toth [12].

In the present paper, we report the application of the Space-Time Conservation Element and Solution Element (CESE) method [17-20] to solve the two-dimensional MHD equations. Four approaches are employed: (i) the original CESE method without any additional treatment for  $\nabla \cdot \mathbf{B} = 0$ , (ii) a simple modification procedure to update the spatial derivatives of  $\mathbf{B}$  after each time marching step such that  $\nabla \cdot \mathbf{B} = 0$  is enforced at all mesh nodes, (iii) an extended CESE method based on the constraint-transport procedure, and (iv) the projection method coupled with the CESE method. The approach (i) is trivial. Nevertheless, its results are comparable with other results by the three other approaches. Approaches (ii) and (iii) are new schemes for  $\nabla \cdot \mathbf{B} = 0$ . Approach (iv), the projection method, is a conventional and reliable approach to impose  $\nabla \cdot \mathbf{B} = 0$ . All results in the present paper compare well with previously published data.

The rest of the paper is arranged as follows. Section 2 illustrates the governing equations. Section 3 provides a brief review of the CESE method for two-spatial-dimensional problems. Section 4 shows the new CESE schemes, i.e., approaches (ii) and (iii), for  $\nabla \cdot \mathbf{B} = 0$ . Section 5 provides the results and discussions. We then offer conclusions and provide cited references.

## 2 Governing Equations

The ideal MHD equations include the continuity, the momentum, the energy, and the magnetic induction equations. In two spatial dimensions, the dimensionless equations can be cast into the following conservative form:

$$\frac{\partial \mathbf{U}}{\partial t} + \frac{\partial \mathbf{F}}{\partial x} + \frac{\partial \mathbf{G}}{\partial y} = 0, \tag{2.1}$$

where

$$\mathbf{U} = (\mathbf{r}, \mathbf{ru}, \mathbf{rv}, \mathbf{rw}, e, B_x, B_y, B_z)^T = (u_1, u_2, u_3, u_4, u_5, u_6, u_7, u_8)^T, \quad (2.2)$$

$$\mathbf{F}(\mathbf{U}) = \begin{pmatrix} \mathbf{ru} \\ \mathbf{ru}^2 + p_0 - B_x^2 \\ \mathbf{ruv} - B_x B_y \\ \mathbf{ruw} - B_x B_z \\ (e + p_0)\mathbf{u} - B_x(uB_x + vB_y + wB_z) \\ 0 \\ uB_y - vB_x \\ uB_z - wB_x \end{pmatrix} = \begin{pmatrix} f_1 \\ f_2 \\ f_3 \\ f_4 \\ f_5 \\ f_6 \\ f_7 \\ f_8 \end{pmatrix}, \quad (2.3)$$

and

$$\mathbf{G}(\mathbf{U}) = \begin{pmatrix} \mathbf{rv} \\ \mathbf{rvu} - B_y B_x \\ \mathbf{rv}^2 + p_0 - B_y^2 \\ \mathbf{rvw} - B_y B_z \\ (e + p_0)\mathbf{v} - B_y(uB_x + vB_y + wB_z) \\ vB_x - uB_y \\ 0 \\ vB_z - wB_y \end{pmatrix} = \begin{pmatrix} g_1 \\ g_2 \\ g_3 \\ g_4 \\ g_5 \\ g_6 \\ g_7 \\ g_8 \end{pmatrix}. \quad (2.4)$$

In the above equations,  $\mathbf{r}$ ,  $p$  and  $e$  are density, pressure and specific total energy, respectively;  $u$ ,  $v$ , and  $w$  are velocity components and  $B_x$ ,  $B_y$  and  $B_z$  are magnetic field components in the  $x$ ,  $y$ , and  $z$  directions, respectively. The total pressure and the specific total energy are

$$p_0 = p + (B_x^2 + B_y^2 + B_z^2)/2, \quad (2.5)$$

$$e = \mathbf{re} + \mathbf{r}(u^2 + v^2 + w^2)/2 + (B_x^2 + B_y^2 + B_z^2)/2. \quad (2.6)$$

For calorically ideal gases, the specific internal energy  $e$  can be expressed as

$$e = \frac{p}{(\mathbf{g}-1)\mathbf{r}} = \frac{RT}{(\mathbf{g}-1)}, \quad (2.7)$$

where  $\mathbf{g}$  is the specific heat ratio,  $T$  is temperature, and  $R$  is the gas constant. To proceed, we apply the chain rule to Eq. (2.1) and obtain

$$\frac{\partial \mathbf{U}}{\partial t} + \mathbf{J}^x \frac{\partial \mathbf{U}}{\partial x} + \mathbf{J}^y \frac{\partial \mathbf{U}}{\partial y} = 0, \quad (2.8)$$

where  $\mathbf{J}^x$  and  $\mathbf{J}^y$  are Jacobian matrices of the spatial fluxes in the  $x$  and  $y$  directions, respectively. The components of the matrices are listed in Appendix. The eigenvalues of matrix  $\mathbf{J}^x$  are  $u \pm c_f^x$ ,  $u \pm c_a^x$ ,  $u \pm c_s^x$ ,  $u$  and  $u$ , where  $c_a^x$ ,  $c_s^x$  and  $c_f^x$  are the speeds of the Alfvén wave, the slow shock wave, and the fast shock wave, respectively, and they are defined as

$$c_a^x = |B_x| / \sqrt{\mathbf{r}}, \quad (2.9)$$

$$c_f^x = \left\{ \frac{1}{2} \left[ c^2 + \frac{\mathbf{B} \cdot \mathbf{B}}{\mathbf{r}} + \sqrt{\left( c^2 + \frac{\mathbf{B} \cdot \mathbf{B}}{\mathbf{r}} \right)^2 - 4 \frac{c^2 B_x^2}{\mathbf{r}}} \right] \right\}^{1/2}, \quad (2.10)$$

$$c_s^x = \left\{ \frac{1}{2} \left[ c^2 + \frac{\mathbf{B} \cdot \mathbf{B}}{\mathbf{r}} - \sqrt{\left( c^2 + \frac{\mathbf{B} \cdot \mathbf{B}}{\mathbf{r}} \right)^2 - 4 \frac{c^2 B_x^2}{\mathbf{r}}} \right] \right\}^{1/2}. \quad (2.11)$$

In Eqs. (2.10-11),  $c = \sqrt{\mathbf{g}p/\mathbf{r}}$  is the speed of sound. Similarly, the eigenvalues of matrix

$\mathbf{J}^y$  are  $v \pm c_f^y$ ,  $v \pm c_a^y$ ,  $v \pm c_s^y$ ,  $v$  and  $v$ , where  $c_a^y$ ,  $c_s^y$  and  $c_f^y$  are defined as

$$c_a^y = |B_y| / \sqrt{\mathbf{r}}, \quad (2.12)$$

$$c_f^y = \left\{ \frac{1}{2} \left[ c^2 + \frac{\mathbf{B} \cdot \mathbf{B}}{r} + \sqrt{\left( c^2 + \frac{\mathbf{B} \cdot \mathbf{B}}{r} \right)^2 - 4 \frac{c^2 B_y^2}{r}} \right] \right\}^{1/2}, \quad (2.13)$$

$$c_s^y = \left\{ \frac{1}{2} \left[ c^2 + \frac{\mathbf{B} \cdot \mathbf{B}}{r} - \sqrt{\left( c^2 + \frac{\mathbf{B} \cdot \mathbf{B}}{r} \right)^2 - 4 \frac{c^2 B_y^2}{r}} \right] \right\}^{1/2}. \quad (2.14)$$

### 3 The CESE Method

The above MHD equations can be expressed as

$$\frac{\partial u_m}{\partial t} + \frac{\partial f_m}{\partial x} + \frac{\partial g_m}{\partial y} = 0, \quad m = 1, 2, \dots, 8, \quad (3.1)$$

where  $u_m$ ,  $f_m$  and  $g_m$  are the entries of the flow variable vector and the flux vectors in the  $x$  and  $y$  directions, respectively, and  $m$  is the index for the equation. Let  $x_1 = x$ ,  $x_2 = y$  and  $x_3 = t$  be the coordinates of a three-dimensional Euclidean space  $E_3$ , Eq. (3.1) becomes a divergence free condition:

$$\nabla \cdot \mathbf{h}_m = 0, \quad m = 1, 2, \dots, 8, \quad (3.2)$$

where  $\mathbf{h}_m = (f_m, g_m, u_m)$  are the current density vector. By using Gauss' divergence theorem in  $E_3$ , we have

$$\int_V \nabla \cdot \mathbf{h}_m dV = \oint_{S(V)} \mathbf{h}_m \cdot d\mathbf{s} = 0, \quad m = 1, 2, \dots, 8, \quad (3.3)$$

where (i)  $S(V)$  is the boundary of an arbitrary space-time region  $V$  in  $E_3$ , and (ii)  $d\mathbf{s} = \mathbf{n} dS$  with  $dS$  and  $\mathbf{n}$ , respectively, are the area and the unit outward normal of a

surface element on  $S(V)$ . The CESE method integrates Eq. (3.3) for the evolving flow variables.

For completeness, we will briefly illustrate the CESE method based on the following three parts: (i) The definition of SE and CE in the space-time domain. (ii) The integration of Eq. (3.3) over a CE to form the algebraic equations for the flow variables at a new time step. (iii) The re-weighting procedure with added artificial damping in calculating the gradients of the flow variables. The discussion of the CESE method here will be based on the modified CESE method for a quadrilateral mesh [19]. To be concise, our discussion of the CESE method will be focused on a uniform quadrilateral mesh.

### 3.1 Definition of Solution Element and Conservation Element

In Fig. 1, the spatial domain is divided into non-overlapping quadrilaterals and any two neighboring quadrilaterals share a common side. The centroid of each quadrilateral is marked by either a hollow circle or a solid circle. Point  $G$ , the centroid of quadrilateral  $ABCD$ , is marked by a solid circle, while the points  $N$ ,  $E$ ,  $W$  and  $S$  are the centroids of the four neighboring quadrilaterals, and are marked by hollow circles. Because of the uniform mesh,  $G$  is also the centroid of polygon  $NAWBSCED$ , which coincides with quadrilateral  $NWSE$ . Let  $j$ ,  $k$  and  $n$  be the indices for  $x$ ,  $y$ , and  $t$ , respectively. Shown in Fig. 2, points  $A$ ,  $B$ ,  $C$ ,  $D$ ,  $N$ ,  $E$ ,  $W$ ,  $S$  and  $G$  are at the time level  $n-1/2$ ; points  $A'$ ,  $B'$ ,  $C'$ ,  $D'$ ,  $N'$ ,  $E'$ ,  $W'$ ,  $S'$  and  $G'$  are at the time level  $n$ ; and points  $A''$ ,  $B''$ ,  $C''$ ,  $D''$ ,  $N''$ ,  $E''$ ,  $W''$ ,  $S''$  and  $G''$  are at the time level  $n+1/2$ .

As shown in Fig. 2, the solution element  $SE(j, k, n)$  associated with point  $G'$  is defined as the union of three quadrilateral planes,  $N'W'S'E'$ ,  $A''ACC''$ ,  $B''BDD''$ , and



their immediate neighborhoods. Its spatial projection is shown in Fig. 1 as the dashed lines. Similarly, associated with points  $N$ ,  $E$ ,  $W$ , and  $S$ , there are four solution elements:  $SE(j, k+1/2, n-1/2)$ ,  $SE(j+1/2, k, n-1/2)$ ,  $SE(j-1/2, k, n-1/2)$ , and  $SE(j, k-1/2, n-1/2)$ . To calculate the unknowns at  $G'$ , the algebraic equations are derived based on space-time flux conservation involved flow solutions at points  $G'$ ,  $N$ ,  $E$ ,  $W$ , and  $S$ , referred to as the solution points. Point  $G'$ , located at  $t = t^n$  is staggered with respect to points  $N$ ,  $E$ ,  $W$ , and  $S$  at  $t = t^{n-1/2}$ .

As shown in Fig. 2, a space-time cylinder can be formed with surfaces associated with  $SE(j, k, n)$  and surfaces associated with one of the four SEs at the time level  $n-1/2$ . For instance, cylinder  $N'A'G'D'NAGD$  is formed by surfaces associated with  $SE(j, k, n)$  and  $SE(j, k+1/2, n-1/2)$ . This cylinder is one of the Basic Conservation Elements (BCE) of point  $G'$ . There are three other BCEs associated with point  $G'$ , i.e.,  $A'W'B'G'AWBG$ ,  $B'S'C'G'BSCG$  and  $C'E'D'G'CEDG$ . The union of these four BCEs forms a Compounded Conservation Element (CCE)  $N'W'S'E'NWSE$  with its top center at point  $G'$ .

### 3.2 The Space-Time Integration

Inside  $SE(j, k, n)$ , the discretized variables and fluxes, denoted with a superscript \*, are assumed to be linear. For  $m = 1, 2, \dots, 8$ , let

$$u_m^*(x, y, t; j, k, n) = (u_m)_{j,k}^n + (u_{mx})_{j,k}^n (x - x_{j,k}) + (u_{my})_{j,k}^n (y - y_{j,k}) + (u_{mt})_{j,k}^n (t - t^n), \quad (3.4)$$

$$f_m^*(x, y, t; j, k, n) = (f_m)_{j,k}^n + (f_{mx})_{j,k}^n (x - x_{j,k}) + (f_{my})_{j,k}^n (y - y_{j,k}) + (f_{mt})_{j,k}^n (t - t^n), \quad (3.5)$$

$$g_m^*(x, y, t; j, k, n) = (g_m)_{j,k}^n + (g_{mx})_{j,k}^n (x - x_{j,k}) + (g_{my})_{j,k}^n (y - y_{j,k}) + (g_{mt})_{j,k}^n (t - t^n), \quad (3.6)$$

where  $(u_m)_{j,k}^n$ ,  $(f_m)_{j,k}^n$ ,  $(g_m)_{j,k}^n$ ,  $(u_{mx})_{j,k}^n$ ,  $(u_{my})_{j,k}^n$ ,  $(u_{mt})_{j,k}^n$ ,  $(f_{mx})_{j,k}^n$ ,  $(f_{my})_{j,k}^n$ ,  $(f_{mt})_{j,k}^n$ ,  $(g_{mx})_{j,k}^n$ ,  $(g_{my})_{j,k}^n$ , and  $(g_{mt})_{j,k}^n$  are flow variables, fluxes, and their first-order derivatives at point  $G'$ . Aided by the chain rule we have

$$(f_{mx})_{j,k}^n = \sum_{l=1}^8 (f_{m,l})_{j,k}^n (u_{lx})_{j,k}^n, \quad m = 1, 2, \dots, 8, \quad (3.7)$$

$$(g_{mx})_{j,k}^n = \sum_{l=1}^8 (g_{m,l})_{j,k}^n (u_{lx})_{j,k}^n, \quad m = 1, 2, \dots, 8 \quad (3.8)$$

$$(f_{my})_{j,k}^n = \sum_{l=1}^8 (f_{m,l})_{j,k}^n (u_{ly})_{j,k}^n, \quad m = 1, 2, \dots, 8 \quad (3.9)$$

$$(g_{my})_{j,k}^n = \sum_{l=1}^8 (g_{m,l})_{j,k}^n (u_{ly})_{j,k}^n, \quad m = 1, 2, \dots, 8 \quad (3.10)$$

where  $(f_{m,l})_{j,k}^n$ ,  $(g_{m,l})_{j,k}^n$  are the  $(m, l)$ th entries of the Jacobian matrixes  $\mathbf{J}^x$  and  $\mathbf{J}^y$  in the  $x$  and  $y$  directions, respectively. To proceed, we assume that  $u_m^*(x, y, t; j, k, n)$ ,  $f_m^*(x, y, t; j, k, n)$  and  $g_m^*(x, y, t; j, k, n)$  satisfy the original MHD equations, Eq. (3.1), at point,  $(j, k, n)$ :

$$(u_{mt})_{j,k}^n = -(f_{mx})_{j,k}^n - (g_{my})_{j,k}^n, \quad m = 1, 2, \dots, 8. \quad (3.11)$$

Aided by Eqs. (3.7) and (3.10), Eq. (3.11) becomes

$$(u_{mt})_{j,k}^n = -\sum_{l=1}^8 (f_{m,l})_{j,k}^n (u_{lx})_{j,k}^n - \sum_{l=1}^8 (g_{m,l})_{j,k}^n (u_{ly})_{j,k}^n, \quad m = 1, 2, \dots, 8, \quad (3.12)$$

Similarly, for  $m = 1, 2, \dots, 8$ , we have

$$(f_{mt})_{j,k}^n = \sum_{l=1}^8 (f_{m,l})_{j,k}^n (u_{lt})_{j,k}^n = - \sum_{l=1}^8 (f_{m,l})_{j,k}^n \sum_{r=1}^8 [(f_{l,r})_{j,k}^n (u_{rx})_{j,k}^n + (g_{l,r})_{j,k}^n (u_{ry})_{j,k}^n], \quad (3.13)$$

$$(g_{mt})_{j,k}^n = \sum_{l=1}^8 (g_{m,l})_{j,k}^n (u_{lt})_{j,k}^n = - \sum_{l=1}^8 (g_{m,l})_{j,k}^n \sum_{r=1}^8 [(f_{l,r})_{j,k}^n (u_{rx})_{j,k}^n + (g_{l,r})_{j,k}^n (u_{ry})_{j,k}^n]. \quad (3.14)$$

Therefore, a set of given values of  $(u_m)_{j,k}^n$ ,  $(u_{mx})_{j,k}^n$  and  $(u_{my})_{j,k}^n$  completely determine the distribution of the flow variables and fluxes, i.e., Eqs., (3.4-6), inside  $SE(j, k, n)$ . Thus the flow variables  $(u_m)_{j,k}^n$  and their spatial gradients  $(u_{mx})_{j,k}^n$  and  $(u_{my})_{j,k}^n$  are the unknowns to be solved in the CESE method.

The time marching scheme to calculate  $(u_m)_{j,k}^n$  is based on integrating Eq. (3.3) over the CCE associated with point  $G'$ . Recall that the CCE is a quadrilateral cylinder with surfaces associated with five different SEs. The top surface, quadrilateral  $N'W'S'E'$  belongs to  $SE(j, k, n)$ ; quadrilaterals  $NAGD$ ,  $N'A'AN$  and  $N'D'DN$  belong to  $SE(j, k+1/2, n-1/2)$ ; quadrilaterals  $WAGB$ ,  $W'A'AW$  and  $W'B'BW$  belong to  $SE(j-1/2, k, n-1/2)$ ; quadrilaterals  $SBGC$ ,  $S'B'BS$  and  $S'C'CS$  belong to  $SE(j, k-1/2, n-1/2)$ ; and quadrilaterals  $EDGC$ ,  $E'C'CE$  and  $E'D'DE$  belong to  $SE(j+1/2, k, n-1/2)$ .

The flux leaving each planar surface of the CCE is equal to the inner product of the current density vector  $\mathbf{h}_m^* = (f_m^*, g_m^*, u_m^*)$ , evaluated at the centroid of the surface, and the surface vector  $\mathbf{s} = \mathbf{nS}$ . For example, the top surface of the CCE is quadrilateral  $N'W'S'E'$  with an area  $S_{top}$  and the centroid is  $G' (x_{j,k}, y_{j,k}, t^n)$ . At the centroid of the top surface of

the CCE, the current density vector  $\mathbf{h}_m^* = \left( (f_m)_{j,k}^n, (g_m)_{j,k}^n, (u_m)_{j,k}^n \right)$ , and the surface vector is  $(0, 0, S_{top})$ . Thus the flux leaving the top surface of the CCE is

$$(FLUX_m)_{top} = (u_m)_{j,k}^n S_{top}, m = 1, 2, \dots, 8. \quad (3.15)$$

Similarly calculation for fluxes through other surfaces of the CCE can be performed. For surfaces associated with  $SE(j, k+1/2, n-1/2)$ , the centroids of surfaces  $NAGD$ ,  $NDD'N'$  and  $NAA'N'$  are denoted as  $(x_N^0, y_N^0, t^{n-1/2})$ ,  $(x_N^1, y_N^1, t^{n-1/4})$  and  $(x_N^2, y_N^2, t^{n-1/4})$ , respectively. Their surface vectors are  $(0, 0, -S_1)$ ,  $(\mathbf{I}_N^{1x}, \mathbf{I}_N^{1y}, 0)$ , and  $(\mathbf{I}_N^{2x}, \mathbf{I}_N^{2y}, 0)$ , where  $S_1$  is the area of quadrilateral  $NAGD$ , and

$$\mathbf{I}_N^{1x} = (y_N - y_D)\Delta t/2, \quad (3.16)$$

$$\mathbf{I}_N^{1y} = (x_D - x_N)\Delta t/2, \quad (3.17)$$

$$\mathbf{I}_N^{2x} = (y_A - y_N)\Delta t/2, \quad (3.18)$$

$$\mathbf{I}_N^{2y} = (x_N - x_A)\Delta t/2. \quad (3.19)$$

The flux leaving each of the three surfaces can be calculated as the inner product of the corresponding flux vector and the surface vector at the surface centroid. By summing up the fluxes, for  $m = 1, 2, \dots, 8$ , we have,

$$\begin{aligned} (FLUX_m)_N &= -S_1 u_m^*(x_N^0, y_N^0, t^{n-1/2}; j, k+1/2, t^{n-1/2}) \\ &\quad + \mathbf{I}_N^{1x} f_m^*(x_N^1, y_N^1, t^{n-1/4}; j, k+1/2, t^{n-1/2}) + \mathbf{I}_N^{1y} g_m^*(x_N^1, y_N^1, t^{n-1/4}; j, k+1/2, t^{n-1/2}) \\ &\quad + \mathbf{I}_N^{2x} f_m^*(x_N^2, y_N^2, t^{n-1/4}; j, k+1/2, t^{n-1/2}) + \mathbf{I}_N^{2y} g_m^*(x_N^2, y_N^2, t^{n-1/4}; j, k+1/2, t^{n-1/2}) \end{aligned} \quad (3.20)$$

Because the solution at the time step  $n-1/2$  is known, the value of this flux can be readily calculated. Similarly, the fluxes leaving surfaces associated with  $SE(j-1/2, k, n-1/2)$ ,  $SE(j,$

$k-1/2$ ,  $n-1/2$ ), and  $SE(j+1/2, k, n-1/2)$  can be readily calculated. For conciseness, we simply name these fluxes as  $(FLUX_m)_W$ ,  $(FLUX_m)_S$  and  $(FLUX_m)_E$ . As a result, the space-time flux conservation over the CCE is

$$(FLUX_m)_{top} + \sum_l^{NEWS} (FLUX_m)_l = 0, m = 1, 2, \dots, 8. \quad (3.21)$$

Note that only the first term in the above equation contains the unknowns to be solved at point  $G'$ . Aided by Eq. (3.15), the flow variables at the current time step  $n$  can be calculated by

$$(u_m)_{j,k}^n = -\frac{\sum_l^{NEWS} (FLUX_m)_l}{S_{top}}, m = 1, 2, \dots, 8. \quad (3.22)$$

### 3.3 Solutions of Flow Variable Gradients

To proceed, we calculate the spatial gradients of the flow variables  $(u_{mx})_{j,k}^n$  and  $(u_{my})_{j,k}^n$ . The calculation is divided into two steps: (i) Finite-differencing the flow variables  $u_m$  at point  $G'$ ,  $N'$ ,  $E'$ ,  $W'$ , and  $S'$ , at  $t = t^n$  to obtain four sets of  $u_{mx}$  and  $u_{my}$ . (ii) Apply a reweighing procedure to the above four sets of  $u_{mx}$  and  $u_{my}$  to determine  $(u_{mx})_{j,k}^n$  and  $(u_{my})_{j,k}^n$  at  $G'$ . In what follows, these two calculation steps are illustrated.

Flow variables  $u_m$  at point  $G'$  are obtained from Eq. (3.22). The flow variables  $u_m$  at four neighbor points  $N'$ ,  $W'$ ,  $S'$  and  $E'$  are obtained by using the Taylor series expansion along the time axis from the time level  $n-1/2$ , i.e., for  $m = 1, 2, \dots, 8$ ,

$$\left(u_m'\right)_l = \left(u_m\right)_l^{n-1/2} + \frac{\Delta t}{2} \left(u_{mt}\right)_l^{n-1/2}, \quad (3.23)$$

where  $l=1, 2, 3$ , and  $4$  denoting point  $N'$ ,  $E'$ ,  $W'$  and  $S'$ , respectively.

The square plane  $N'E'S'W'$  is divided into four triangles;  $N'W'G'$ ,  $W'S'G'$ ,  $S'E'G'$ , and  $E'N'G'$ . In each triangle, we finite-difference  $u_m$  at the three vertices to obtain the flow variable gradient  $\left(u_{mx}\right)_{j,k}^n$  and  $\left(u_{my}\right)_{j,k}^n$ . Consider triangle  $\Delta N'W'G'$ , the flow variable gradient at its centroid can be expressed as,

$$\left(u_{mx}^{(1)}\right)_{G'} = \Delta_x / \Delta, \quad (3.24)$$

$$\left(u_{my}^{(1)}\right)_{G'} = \Delta_y / \Delta, \quad (3.25)$$

where

$$\Delta_x = \begin{vmatrix} \left(u_m'\right)_{N'} - \left(u_m\right)_{G'} & y_N - y_G \\ \left(u_m'\right)_{W'} - \left(u_m\right)_{G'} & y_W - y_G \end{vmatrix}, \quad (3.26)$$

$$\Delta_y = \begin{vmatrix} \left(u_m'\right)_{N'} - \left(u_m\right)_{G'} & x_G - x_N \\ \left(u_m'\right)_{W'} - \left(u_m\right)_{G'} & x_G - x_W \end{vmatrix}, \quad (3.27)$$

$$\Delta = \begin{vmatrix} x_N - x_G & y_N - y_G \\ x_W - x_G & y_W - y_G \end{vmatrix}, \quad (3.28)$$

and

$$\left(u_m\right)_{G'} = \left(u_m\right)_{j,k}^n. \quad (3.29)$$

For triangles  $\Delta W'S'G'$ ,  $\Delta S'E'G'$  and  $\Delta E'N'G'$ , the flow variable gradients at their centroids, denoted by  $(\mathbf{u}_{mx}^{(2)})_{G'}$ ,  $(\mathbf{u}_{my}^{(2)})_{G'}$ ,  $(\mathbf{u}_{mx}^{(3)})_{G'}$ ,  $(\mathbf{u}_{my}^{(3)})_{G'}$ ,  $(\mathbf{u}_{mx}^{(4)})_{G'}$  and  $(\mathbf{u}_{my}^{(4)})_{G'}$ , can be obtained in a similar way.

To proceed, a re-weighting procedure is applied to the four sets of flow variable gradients to obtain the final flow variable gradient at  $G'$ , i.e., for  $m = 1, 2, \dots, 8$ ,

$$(\mathbf{u}_{mx})_{j,k}^n = \sum_{l=1}^4 [(W_m^l)^a (\mathbf{u}_{mx}^{(l)})_{G'}] / \sum_{l=1}^4 (W_m^l)^a, \quad (3.30)$$

$$(\mathbf{u}_{my})_{j,k}^n = \sum_{l=1}^4 [(W_m^l)^a (\mathbf{u}_{my}^{(l)})_{G'}] / \sum_{l=1}^4 (W_m^l)^a, \quad (3.31)$$

where

$$W_m^l = \prod_{q=1, q \neq l}^4 W_m^q, \quad \text{for } l = 1, 2, 3, 4, \quad (3.32)$$

and

$$W_m^q = \sqrt{[(\mathbf{u}_{mx}^{(q)})_{G'}]^2 + [(\mathbf{u}_{my}^{(q)})_{G'}]^2}. \quad (3.33)$$

For shock capturing,  $\mathbf{a} = 1$ , or  $2$ , is a prescribed constant. For flows without shock, we let  $\mathbf{a} = 0$ . As such, Eqs. (3.30-31) reduce to the standard central-differencing method.

#### 4 Extended CESE Schemes for $\tilde{\mathbf{N}} \times \mathbf{B} = \mathbf{0}$

In this section, we illustrate two new CESE schemes for  $\tilde{\mathbf{N}} \times \mathbf{B} = \mathbf{0}$ : Schemes I and Schemes II. Both schemes are built based on special features of the original CESE method. Scheme I takes advantage of the fact that the flow variable gradients  $(\mathbf{u}_{mx})_{j,k}^n$  and

$(u_{my})_{j,k}^n$  are directly used as the unknowns and they march in time hand-in-hand with the flow variables  $(u_m)_{j,k}^n$ . Scheme I is a simple adjustment to the calculation of  $(u_{mx})_{j,k}^n$  and  $(u_{my})_{j,k}^n$  such that  $\tilde{\mathbf{N}} \times \mathbf{B} = 0$  is satisfied at all mesh points after each time marching step.

Scheme II takes advantage of staggered mesh arrangement in the original CESE method. By a simple adjustment of the mesh nodes employed in calculating the magnetic flux, we ensure the satisfaction of  $\tilde{\mathbf{N}} \times \mathbf{B} = 0$  at all solution points. In what follows, we report these two schemes.

#### 4.1 Scheme I

As illustrated in the above section, the flow variables  $(u_m)_{j,k}^n$  are calculated by space-time flux conservation i.e., Eq. (3.22), over a CCE with its top center at point  $(j, k, n)$ , while the flow variable gradients  $(u_{mx})_{j,k}^n$  and  $(u_{my})_{j,k}^n$  are calculated by a combination of a central differencing and a reweighing procedure. In Scheme I, we first follow the above CESE algorithm to calculate the flow variables and their spatial gradients. After each time marching step, a corrector step is applied to adjust the values of  $\left(\frac{\partial B_x}{\partial x}\right)_{j,k}^n$  and

$\left(\frac{\partial B_y}{\partial y}\right)_{j,k}^n$ . The calculated results of all other unknowns remain intact. Note that

$\left(\frac{\partial B_x}{\partial x}\right)_{j,k}^n$  and  $\left(\frac{\partial B_y}{\partial y}\right)_{j,k}^n$  are denoted as  $(u_{5x})_{j,k}^n$  and  $(u_{6y})_{j,k}^n$  in Eq. (2.2). The adjustments to

these two terms are



$$\left(u_{5x}\right)_{j,k}^{new} = \left(u_{5x}\right)_{j,k}^n - \frac{1}{2} \left[ \left(u_{5x}\right)_{j,k}^n + \left(u_{6y}\right)_{j,k}^n \right], \quad (4.1)$$

$$\left(u_{6y}\right)_{j,k}^{new} = \left(u_{6y}\right)_{j,k}^n - \frac{1}{2} \left[ \left(u_{5x}\right)_{j,k}^n + \left(u_{6y}\right)_{j,k}^n \right], \quad (4.2)$$

where the updated gradient is denoted by the superscript *new*. By adding the two equations above, we yield

$$\left(u_{5x}\right)_{j,k}^{new} + \left(u_{6y}\right)_{j,k}^{new} = 0. \quad (4.3)$$

That is, with the additional treatment for  $\left(\frac{\partial B_x}{\partial x}\right)_{j,k}$  and  $\left(\frac{\partial B_y}{\partial y}\right)_{j,k}$  by Eqs. (4.1-2), the constraint  $(\nabla \cdot \mathbf{B})_{j,k} = 0$  is satisfied at each mesh node in each time marching step.

## 4.2 Scheme II

Scheme II is based on a specially defined SE for solving the magnetic induction equations. As illustrated in Fig. 3, the Special Conservation Element (SCE) associated with point  $G'$  is defined as quadrilateral  $P'Q'R'T'PQRT$ , which composes of six planes:  $P'Q'R'T'$ ,  $P'Q'QP$ ,  $Q'R'RQ$ ,  $R'T'TR$ ,  $T'P'PT$  and  $PQRT$ . The six planes are referred to as Special Solution Elements (SSE). The SSE and SCE are defined for solving magnetic field components  $B_x$  and  $B_y$  only. Shown in Fig. 3, the solution points  $N'$ ,  $E'$ ,  $W'$ , and  $S'$  surrounding  $G'$  are at the middle of line segments  $P'Q'$ ,  $P'T'$ ,  $Q'R'$  and  $R'T'$ , respectively. Thus the SCE here includes a space-time region larger than the original CCE.

To proceed, the SSEs,  $P'Q'R'T'$  and  $PQRT$ , are defined to be associated with the solution points  $G'$  and  $G$ , respectively. Similarly, the SSEs,  $P'Q'QP$ ,  $Q'R'RQ$ ,  $R'T'TR$

and  $T'P'PT$  are associated with the solution points  $N$ ,  $W$ ,  $S$  and  $E$ , respectively. Inside SSEs, the profiles of  $B_x$  and  $B_y$  follow the first-order Taylor series expansion. For example, we consider SSE  $P'Q'QP$  associated with the solution point  $N$ :

$$u_m^*(x, y, t; j, k + 1/2, n - 1/2) = (u_m)_{j,k+1/2}^{n-1/2} + (u_{mx})_{j,k+1/2}^{n-1/2} (x - x_{j,k+1/2}) + (u_{my})_{j,k+1/2}^{n-1/2} (y - y_{j,k+1/2}) + (u_{mt})_{j,k+1/2}^{n-1/2} (t - t^{n-1/2}), \quad (4.4)$$

$$f_m^*(x, y, t; j, k + 1/2, n - 1/2) = (f_m)_{j,k+1/2}^{n-1/2} + (f_{mx})_{j,k+1/2}^{n-1/2} (x - x_{j,k+1/2}) + (f_{my})_{j,k+1/2}^{n-1/2} (y - y_{j,k+1/2}) + (f_{mt})_{j,k+1/2}^{n-1/2} (t - t^{n-1/2}), \quad (4.5)$$

$$g_m^*(x, y, t; j, k + 1/2, n - 1/2) = (g_m)_{j,k+1/2}^{n-1/2} + (g_{mx})_{j,k+1/2}^{n-1/2} (x - x_{j,k+1/2}) + (g_{my})_{j,k+1/2}^{n-1/2} (y - y_{j,k+1/2}) + (g_{mt})_{j,k+1/2}^{n-1/2} (t - t^{n-1/2}), \quad (4.6)$$

where  $m = 6$  and  $7$ . Similar discretization procedure is employed in the other SSEs.

To proceed, we perform numerical integration of the magnetic induction equations in  $x$  and  $y$  directions over the SCE based on the above discretization scheme for the SSEs. The magnetic induction equations can be reformulated as

$$\frac{\partial B_x}{\partial t} + \frac{\partial \Omega}{\partial y} = 0, \quad (4.7)$$

$$\frac{\partial B_y}{\partial t} - \frac{\partial \Omega}{\partial x} = 0, \quad (4.8)$$

where  $\mathbf{W} = vB_x - uB_y$ . Integrating Eqs. (4.7-8) over the SCE, we have

$$\oint_{S(V)} (0, \Omega, B_x) \cdot d\mathbf{s} = 0, \quad (4.9)$$

$$\oint_{S(V)} (-\Omega, 0, B_y) \cdot d\mathbf{s} = 0. \quad (4.10)$$

Consider Eq. (4.9), flux leaving plane  $P'Q'R'T'$  is

$$FLUX_{P'Q'R'T'} = \Delta x \Delta y (B_x)_{j,k}^n. \quad (4.11)$$

Flux leaving plane  $PQRT$  is

$$FLUX_{PQRT} = -\Delta x \Delta y (B_x)_{j,k}^{n-1/2}. \quad (4.12)$$

Flux leaving plane  $P'Q'QP$  is

$$FLUX_{P'Q'QP} = \frac{\Delta x \Delta t}{2} \left[ (\Omega)_{j,k+1/2}^{n-1/2} + \frac{\Delta t}{4} (\Omega_t)_{j,k+1/2}^{n-1/2} \right] = \frac{\Delta x \Delta t}{2} (\Omega)_{j,k+1/2}^{n-1/4}. \quad (4.13)$$

Flux leaving plane  $R'T'TR$  is

$$FLUX_{R'T'TR} = -\frac{\Delta x \Delta t}{2} \left[ (\Omega)_{j,k-1/2}^{n-1/2} + \frac{\Delta t}{4} (\Omega_t)_{j,k-1/2}^{n-1/2} \right] = -\frac{\Delta x \Delta t}{2} (\Omega)_{j,k-1/2}^{n-1/4}. \quad (4.14)$$

Fluxes leaving planes  $Q'R'RQ$  and  $T'P'PT$  are zero,

$$FLUX_{Q'R'RQ} = 0, \quad (4.15)$$

$$FLUX_{T'P'PT} = 0. \quad (4.16)$$

The flux balance over SCE is

$$FLUX_{P'Q'R'T'} + FLUX_{PQRT} + FLUX_{P'Q'QP} + FLUX_{Q'R'RQ} + FLUX_{R'T'TR} + FLUX_{T'P'PT} = 0. \quad (4.17)$$

Substituting Eqs. (4.11-16) into Eq. (4.17), we have

$$(B_x)_{j,k}^n = (B_x)_{j,k}^{n-1/2} + \frac{\Delta t}{2\Delta y} \left[ (\Omega)_{j,k-1/2}^{n-1/4} - (\Omega)_{j,k+1/2}^{n-1/4} \right]. \quad (4.18)$$

Similarly, integration of Eq. (4.10) over SCE gives

$$(B_y)_{j,k}^n = (B_y)_{j,k}^{n-1/2} + \frac{\Delta t}{2\Delta x} \left[ (\Omega)_{j+1/2,k}^{n-1/4} - (\Omega)_{j-1/2,k}^{n-1/4} \right]. \quad (4.19)$$

For SCEs associated with points  $E'$  and  $W'$ , we have

$$(B_x)_{j+1/2,k}^n = (B_x)_{j+1/2,k}^{n-1/2} + \frac{\Delta t}{2\Delta y} \left[ (\Omega)_{j+1/2,k-1/2}^{n-1/4} - (\Omega)_{j+1/2,k+1/2}^{n-1/4} \right]. \quad (4.20)$$

$$(B_x)_{j-1/2,k}^n = (B_x)_{j-1/2,k}^{n-1/2} + \frac{\Delta t}{2\Delta y} \left[ (\Omega)_{j-1/2,k-1/2}^{n-1/4} - (\Omega)_{j-1/2,k+1/2}^{n-1/4} \right]. \quad (4.21)$$

For SCEs associated with points  $N'$  and  $S'$ , we have

$$(B_y)_{j,k+1/2}^n = (B_y)_{j,k+1/2}^{n-1/2} + \frac{\Delta t}{2\Delta x} \left[ (\Omega)_{j+1/2,k+1/2}^{n-1/4} - (\Omega)_{j-1/2,k+1/2}^{n-1/4} \right]. \quad (4.22)$$

$$(B_y)_{j,k-1/2}^n = (B_y)_{j,k-1/2}^{n-1/2} + \frac{\Delta t}{2\Delta x} \left[ (\Omega)_{j+1/2,k-1/2}^{n-1/4} - (\Omega)_{j-1/2,k-1/2}^{n-1/4} \right]. \quad (4.23)$$

At point  $G'$ , we obtain  $(\partial B_x / \partial x)$  and  $(\partial B_y / \partial y)$  as

$$\left( \frac{\partial B_x}{\partial x} \right)_{j,k}^n = \frac{(B_x)_{j+1/2,k}^n - (B_x)_{j-1/2,k}^n}{\Delta x}, \quad (4.24)$$

$$\left( \frac{\partial B_y}{\partial y} \right)_{j,k}^n = \frac{(B_y)_{j,k+1/2}^n - (B_y)_{j,k-1/2}^n}{\Delta y}. \quad (4.25)$$

Aided by Eqs. (4.20-23) we have

$$(\nabla \cdot \mathbf{B})_{j,k}^n = \frac{(B_x)_{j+1/2,k}^n - (B_x)_{j-1/2,k}^n}{\Delta x} - \frac{(B_y)_{j,k+1/2}^n - (B_y)_{j,k-1/2}^n}{\Delta y} = (\nabla \cdot \mathbf{B})_{j,k}^{n-1/2}. \quad (4.26)$$

That is, if  $(\nabla \cdot \mathbf{B})_{j,k}^{n-1/2} = 0$ ,  $(\nabla \cdot \mathbf{B})_{j,k}^n = 0$ .

Based on the use of the above SSE and SCE, this extended CESE scheme is proposed to solve  $B_x$ ,  $B_y$ ,  $\partial B_x/\partial x$  and  $\partial B_y/\partial y$  at point  $G'$ . All other variables are calculated by using the original CESE scheme as illustrated in Section 3.

## 5 Results and Discussions

In this section, we report results obtained from the CESE schemes. Section 5.1 presents the two-dimensional results of a MHD shock tube problem. Section 5.2 shows the solution of a MHD vortex problem, which is a real two-dimensional problem. For the two problems, we employ the new CESE schemes for maintaining  $\nabla \cdot \mathbf{B} = 0$ . Moreover, for the MHD vortex problem, we also employ the projection procedure, i.e., the Poisson solver, for maintaining  $\nabla \cdot \mathbf{B} = 0$ .

### 5.1 A Rotated Shock Tube Problem

In a one-dimensional problem,  $\nabla \cdot \mathbf{B} = 0$  is automatically satisfied. A common practice to assess multi-dimensional solvers for  $\nabla \cdot \mathbf{B} = 0$  is to perform two-dimensional calculation of an inherently one-dimensional problems formulated in the rotated coordinates such that the one dimensionality of the flow is not aligned with the numerical mesh and  $\nabla \cdot \mathbf{B} = 0$  may not be easily satisfied. As such, the degree of deficiency in satisfying  $\nabla \cdot \mathbf{B} = 0$  can be straightforwardly judged by direct comparison between the two-dimensional results with the corresponding one-dimensional result. As shown in Fig. 4, the computation is conducted in the rectangular domain OABC. The one-dimensional problem is defined along the  $\mathbf{x}$ -direction. Through coordinate rotation, flow variables in the  $x$ - $y$  coordinates can be transformed to be in the  $\mathbf{x}$ - $\mathbf{h}$  coordinates, and vice versa.

The initial condition, defined along  $\mathbf{x}$ -direction, consists of two distinct states:

$$(\mathbf{r}, u, v, p, B_h, B_z) = \begin{cases} (1, 10, 0, 20, 5/\sqrt{4p}, 5/\sqrt{4p}) & \text{for left} \\ (1, -10, 0, 1, 5/\sqrt{4p}, 5/\sqrt{4p}) & \text{for right} \end{cases},$$

with  $\mathbf{g} = 5/3$ ,  $w = 0$ , and  $B_z = 0$ . The flow condition and computational parameters are taken from Toth [12]. The computational domain is  $(x, y) \in [0, 1] \times [0, 2/N]$ , where  $N$  is the grid point in  $x$  direction and set to  $N = 256$ . The rotated angle is set to  $\tan^{-1} 2 \approx 63.43^\circ$ . A periodic condition is imposed in the  $\mathbf{h}$  direction. The computation is up to  $t = 0.08/\sqrt{5}$ , and the computational domain is covered by a mesh of  $256 \times 2$  grid points.

Figure 5 shows results by the original CESE scheme, in which dots denote the present solution and solid lines represent one-dimensional solution in Toth [12]. The right-moving waves include a fast shock, a slow shock and a contact discontinuity. The left-moving waves include a fast shock and a slow rarefaction wave. Favorable comparison is found between our present two-dimensional results and the one-dimensional results. We also employed the new schemes proposed in Section 4 for this problem. Figure 6 shows the comparison of the pressure and magnetic field component  $B_h$  profiles obtained by using (i) the original CESE scheme, (ii) the scheme I with a simple adjustment and (iii) the scheme II based on the constraint-transport procedure. For shock capturing, there is no obvious difference between the original CESE scheme and the new schemes.

Analytically,  $B_x$  is constant along the  $\mathbf{x}$  direction. Figure 7 shows the  $B_x$  profiles calculated by the three different CESE schemes. We observe oscillations around the moving shocks. The oscillations with the original scheme are smaller than that with

scheme I, and are comparable with that with scheme II. Away from shocks, the solutions are smooth.

The same assessment was conducted by Toth [12] by using several special treatments for  $\nabla \cdot \mathbf{B} = 0$ , including the 8-wave method, various versions of the constraint transport methods, and projection method. Refer to Fig. 11 in [12], oscillations of  $B_x$  occur around shocks for all approaches employed. Comparing with the results shown by Toth [12], the magnitudes of  $B_x$  oscillations near the moving shocks calculated by the present three CESE methods are much smaller. Moreover, as shown in Fig. 14 of Toth [12], spurious oscillations of other variable were also observed. In our case, as shown in Fig. 6, no oscillation is observed in present results. Without using a special treatment for  $\nabla \cdot \mathbf{B} = 0$ , the calculated results compare favorably with one-dimensional data. With the use of special treatments for  $\nabla \cdot \mathbf{B} = 0$ , i.e., Scheme I and II, illustrated in Section 4, no obvious improvement is observed.

## 5.2 The MHD Vortex Problem

In this subsection, we report the numerical solution of a MHD vortex problem by Orszag and Tang [21]. The same problem has been employed by Jiang and Wu [4], Tang and Xu [11], and Toth [12] for assessing the numerical treatments for  $\nabla \cdot \mathbf{B} = 0$ . In particular, Jiang and Wu [4] reported numerical instability if the projection procedure was not used.

The initial conditions of the flow field are

$$\begin{aligned} \mathbf{r}(x, y, 0) &= \mathbf{g}^2, & p(x, y, 0) &= \mathbf{g} \\ u(x, y, 0) &= -\sin y, & v(x, y, 0) &= \sin x, & w(x, y, 0) &= 0, \\ B_x(x, y, 0) &= -\sin y, & B_y(x, y, 0) &= \sin 2x, & B_z(x, y, 0) &= 0 \end{aligned}$$

where the specific heat ratio  $\mathbf{g} = 5/3$ . The computational domain is  $[0, 2\mathbf{p}] \times [0, 2\mathbf{p}]$ . Periodic boundary condition is imposed on boundaries in both  $x$ - and  $y$ -directions. We use a uniform mesh of  $193 \times 193$  grid nodes. The same mesh was used by Jiang and Wu [4] and Tang and Xu [11].

Figs. 8 shows the pressure contours of the present CESE results at  $t = 0.5, 2, \text{ and } 3$ , respectively. The results here are calculated by using the original CESE method. Although not shown, the results calculated by using Schemes I and II are virtually the same in these contour plots. To assess the accuracy of the present results, the employed contour levels are exactly the same as that used by Jiang and Wu [4], i.e., 12 equally spaced contour levels ranging from 1.0 to 5.8 for  $t = 0.5$ , from 0.14 to 6.9 for  $t = 2$ , and from 0.36 to 6.3 for  $t = 3$ . Although not shown in the present paper, side-by-side comparisons between the present results and Jiang and Wu's results showed no obvious difference.

For quantitative details of the calculated results, Fig. 9 shows the pressure profiles along the line of  $y = 0.625\pi$  at time  $t = 0.5, 2 \text{ and } 3$ , calculated by using the three CESE schemes: the original scheme and the extended schemes I and II. For  $t = 0.5$ , there is no difference between the results by the three schemes. At  $t = 2$ , result by Scheme II showed a more pronounced gradient near  $x = 5.5$ . For  $t = 3$ , small differences could be discerned on the left end of the plot. In Fig. 9c, result reported by Tang and Xu [11] is also plotted. No obvious difference can be observed between their results and the present results by the original CESE scheme and Scheme I.



We remark that in scheme II, there is no damping treatment for discontinuity in calculating the first-order derivatives  $\partial B_x/\partial x$  and  $\partial B_y/\partial y$ . Moreover, the mesh stencil for calculating  $B_x$ ,  $B_y$ ,  $\partial B_x/\partial x$ , and  $\partial B_y/\partial y$  are larger than that the one (the original CESE method) used for the rest of unknowns due to the use of SSE and SCE. Figure 10 shows time history of the magnetic energy of the whole flow field. Solid line is the result from the original CESE method, and dots are Tang and Xu's results in [11].

To further investigate the capability of the CESE method for  $\nabla \cdot \mathbf{B} = 0$ , we adopt the projection method and solve the Poisson equation at every time step,

$$\nabla^2 \phi + \nabla \cdot \mathbf{B} = 0, \quad (5.1)$$

where  $\mathbf{B}$  is obtained from the CESE method described in Section 3. According to the mesh arrangement shown in Fig. 1, Eqn. (5.1) is discretized as,

$$\frac{\mathbf{f}_{j+1/2,k} - 2\mathbf{f}_{j,k} + \mathbf{f}_{j-1/2,k}}{(\Delta x/2)^2} + \frac{\mathbf{f}_{j,k+1/2} - 2\mathbf{f}_{j,k} + \mathbf{f}_{j,k-1/2}}{(\Delta y/2)^2} = -(\nabla \cdot \mathbf{B})_{j,k}. \quad (5.2)$$

An implicit solver is employed to solve the above equation, and the magnetic field  $\mathbf{B}$  is updated by,

$$\mathbf{B}^c = \mathbf{B} + \nabla \phi. \quad (5.3)$$

The updated  $\mathbf{B}^c$  is then used to march the flow solution to the next time step. Fig. 11 shows pressure profiles along  $y = 0.625\pi$  at  $t = 3$  with and without the projection procedure. We observe no obvious improvement by employing the projection procedure.

## 6. Conclusions

In this paper, we report the extension of the CESE method for solving the ideal MHD equations in two-spatial dimensions with emphasis on satisfying the  $\nabla \cdot \mathbf{B} = 0$  constraint.

Three numerical treatments are developed (i) a simple algebraic adjustment of  $\left(\frac{\partial B_x}{\partial x}\right)_{j,k}^n$

and  $\left(\frac{\partial B_y}{\partial y}\right)_{j,k}^n$  after each time marching step to satisfy  $\nabla \cdot \mathbf{B} = 0$ , (ii) an extended CESE

method based on the constraint-transport method to calculate the magnetic field, and (iii) a projection method by coupling a Poisson solver with the original CESE method. To demonstrate the capabilities of the CESE methods, two benchmark problems are calculated and compared with the previously published results, including a rotated MHD shock tube problem and a MHD vortex problem. All present results produced by the new CESE schemes compare favorably with the previous results. Moreover, we demonstrate that the original CESE method could be directly used to calculate the MHD equations without any difficulty. For the benchmark problems, the results are as accurate as that produced by using sophisticated special treatments.

## References

1. M. Brio and C. C. Wu, An upwind difference scheme for the equations of ideal magnetohydrodynamics, *Journal of Computational Physics*, 75, 400-422 (1988).
2. L. Zachary, A. Malagoli and P. A. Colella, A high-order Godunov method for multidimensional ideal magnetohydrodynamics, *SIAM Journal of Scientific Computation*, 15, 263-285, (1994).

3. R. S. Myong and P. L. Roe, On Godunov type schemes for magnetohydrodynamics, *Journal of Computational Physics*, 147, 545-564 (1998).
4. G. -S. Jiang, C. C. Wu, A high-order WENO finite difference scheme for the equations of ideal magneto-hydrodynamics, *Journal of Computational Physics*, 150, 561-594 (1999).
5. J .P. Brackbill and D.C. Barnes, The effect of nonzero  $\nabla \cdot \mathbf{B}$  on the numerical solution of the magnetohydrodynamic equations, *Journal of Computational Physics*, 35, 426-430 (1980).
6. K. G. Powell, An approximate Riemann solver for magneto-hydro-dynamics, ICASE Report 94-24 (1994).
7. C .R. Evans, and J. F. Hawley, Simulation of magnetohydrodynamic flows: a constrained transport Method, *Astrophys. J.*, 332, 659-677 (1988).
8. W. Dai, and P. R. Woodward, A simple finite difference scheme for multidimensional magnetohydrodynamical equations, *Journal of Computational Physics*, 142, 331-369 (1998).
9. D. S. Balsara and D. S, Spice, A staggered mesh algorithm using high order Godunov fluxes to ensure solenoidal magnetic fields in magnetohydrodynamic simulations, *Journal of Computational Physics*, 149, 270-292 (1999).
10. D. Ryu, F. T. Miniati, W. Jones and A. Frank, A Divergence-free upwind code for multidimensional magnetohydrodynamic flows, *Astrophys. J.*, 509, 244-255 (1998).
11. H. -Z. Tang and K. Xu, A high-order gas-kinetic method for multidimensional ideal magnetohydrodynamics, *Journal of Computational Physics*, 165, 69-88(2000).

12. G. Tóth, The constraint  $\nabla \cdot \mathbf{B} = 0$  in shock capturing magneto-hydrodynamics codes, *Journal of Computational Physics*, 161, 605-652 (2000).
13. P. Londrillo and L. Del Zanna, On the divergence-free condition in Godunov-type schemes for ideal magnetohydrodynamics: the upwind constrained transport method, *Journal of Computational Physics*, 195, 17-48 (2004).
14. P. R. Peyrard and P. Villedieu, A Roe scheme for ideal MHD equations on 2D adaptively refined triangular grids, *Journal of Computational Physics*, 150, 373-393 (1999).
15. S.C. Chang and W. M. To, A new numerical framework for solving conservation laws – the method of space-time conservation element and solution element, *NASA TM 104498* (1991).
16. S. C. Chang, The method of space-time conservation element and solution element—a new approach for solving the Navier-Stokes and the Euler Equations, *Journal of Computational Physics*, 119, 295-324 (1995).
17. S. C. Chang, X. Y. Wang and C.Y. Chow, The space-time conservation element and solution element method: a new high-resolution and genuinely multidimensional paradigm for solving conservation laws, *Journal of Computational Physics*, 156, 89-136 (1999).
18. X. Y. Wang and S. C. Chang, A 2D non-splitting unstructured triangular mesh Euler solver based on the space-time conservation element and solution element method, *Computational Fluid Dynamics Journal*, 8, 309-325 (1999).

19. Z.C. Zhang, S. T. Yu, and S. C. Chang, A space-time conservation element and solution element method for solving the two- and three-dimensional unsteady Euler equations using quadrilateral and hexahedral meshes, *Journal of Computational Physics*, 175, 168-199 (2002).
20. M.J. Zhang, S. C. Lin, S. T. Yu, S. C. Chang and I. Blankson, Application of the space-time conservation element and solution element method to the ideal magnetohydrodynamics equations, *AIAA paper 2002-3888*, (2002).
21. A. Orszag, and C. M. Tang, Small-scale structure of two-dimensional magnetohydrodynamic turbulence, *Journal of Fluid Mechanics*, 90, 129-145 (1979).

## Appendix: Jacobian Matrixes

$$\mathbf{J}^x = \frac{\partial \mathbf{F}}{\partial \mathbf{U}} = \begin{bmatrix} 0 & 1 & 0 & 0 & 0 & 0 & 0 & 0 & 0 \\ \frac{\mathbf{g}-3}{2}u^2 + \frac{\mathbf{g}-1}{2}(v^2 + w^2) & (3-\mathbf{g})u & (1-\mathbf{g})v & (1-\mathbf{g})w & \mathbf{g}-1 & -\mathbf{g}B_x & (2-\mathbf{g})B_y & (2-\mathbf{g})B_z & 0 \\ -uv & v & u & 0 & 0 & -B_y & -B_x & 0 & 0 \\ -uw & w & 0 & u & 0 & -B_z & 0 & -B_x & 0 \\ A_1 & A_2 & A_3 & A_4 & A_5 & A_6 & A_7 & A_8 & 0 \\ 0 & 0 & 0 & 0 & 0 & 0 & 0 & 0 & 0 \\ -\frac{uB_y - vB_x}{\mathbf{r}} & \frac{B_y}{\mathbf{r}} & -\frac{B_x}{\mathbf{r}} & 0 & 0 & -v & u & 0 & 0 \\ -\frac{uB_z - wB_x}{\mathbf{r}} & \frac{B_z}{\mathbf{r}} & 0 & -\frac{B_x}{\mathbf{r}} & 0 & -w & 0 & u & 0 \end{bmatrix} \quad (\text{A.1})$$

where

$$A_1 = -\mathbf{g} \frac{ue}{\mathbf{r}} + (\mathbf{g}-1)u(u^2 + v^2 + w^2) + \frac{\mathbf{g}-2}{2}u \frac{B_y^2 + B_z^2}{\mathbf{r}} + \frac{\mathbf{g}}{2}u \frac{B_x^2}{\mathbf{r}} + B_x \frac{vB_y + wB_z}{\mathbf{r}}, \quad (\text{A.2a})$$

$$A_2 = \mathbf{g} \frac{e}{\mathbf{r}} + \frac{3}{2}(1-\mathbf{g})u^2 + \frac{1-\mathbf{g}}{2}(v^2 + w^2) - \frac{\mathbf{g}-2}{2} \frac{B_y^2 + B_z^2}{\mathbf{r}} - \frac{\mathbf{g}}{2} \frac{B_x^2}{\mathbf{r}}, \quad (\text{A.2b})$$

$$A_3 = (1-\mathbf{g})uv - \frac{B_x B_y}{\mathbf{r}}, \quad (\text{A.2c})$$

$$A_4 = (1-\mathbf{g})uw - \frac{B_x B_z}{\mathbf{r}}, \quad (\text{A.2d})$$

$$A_5 = \mathbf{g}u, \quad (\text{A.2e})$$

$$A_6 = -\mathbf{g}uB_x - (vB_y + wB_z), \quad (\text{A.2f})$$

$$A_7 = -vB_x + (2-\mathbf{g})uB_y, \quad (\text{A.2g})$$

and

$$A_8 = -wB_x + (2-g)uB_z. \quad (\text{A.2h})$$

Matrix

$$\mathbf{J}^y = \frac{\partial \mathbf{G}}{\partial \mathbf{U}} = \begin{bmatrix} 0 & 0 & 1 & 0 & 0 & 0 & 0 & 0 \\ uv & v & u & 0 & 0 & -gB_y & -gB_x & 0 \\ \frac{g-3}{2}v^2 + \frac{g-1}{2}(u^2 + w^2) & (1-g)u & (3-g)v & (1-g)w & g-1 & (2-g)B_x & gB_y & gB_z \\ -vw & 0 & w & v & 0 & 0 & -B_z & -B_y \\ B_1 & B_2 & B_3 & B_4 & B_5 & B_6 & B_7 & B_8 \\ \frac{uB_y - vB_x}{\mathbf{r}} & -\frac{B_y}{\mathbf{r}} & \frac{B_x}{\mathbf{r}} & 0 & 0 & v & u & 0 \\ 0 & 0 & 0 & 0 & 0 & 0 & 0 & 0 \\ -\frac{vB_z - wB_y}{\mathbf{r}} & 0 & \frac{B_z}{\mathbf{r}} & -\frac{B_y}{\mathbf{r}} & 0 & 0 & -w & v \end{bmatrix} \quad (\text{A.3})$$

where

$$B_1 = -g \frac{ve}{\mathbf{r}} + (g-1)v(u^2 + v^2 + w^2) + \frac{g-2}{2}v \frac{B_x^2 + B_z^2}{\mathbf{r}} + \frac{g}{2}u \frac{B_y^2}{\mathbf{r}} + B_y \frac{uB_x + wB_z}{\mathbf{r}}, \quad (\text{A.4a})$$

$$B_2 = (1-g)uv - \frac{B_x B_y}{\mathbf{r}}, \quad (\text{A.4b})$$

$$B_3 = g \frac{e}{\mathbf{r}} + \frac{3}{2}(1-g)v^2 + \frac{1-g}{2}(u^2 + w^2) - \frac{g-2}{2} \frac{B_x^2 + B_z^2}{\mathbf{r}} - \frac{g}{2} \frac{B_y^2}{\mathbf{r}}, \quad (\text{A.4c})$$

$$B_4 = (1-g)vw - \frac{B_y B_z}{\mathbf{r}}, \quad (\text{A.4d})$$

$$B_5 = gv, \quad (\text{A.4e})$$

$$B_6 = (2 - \mathbf{g})vB_x - uB_y, \quad (\text{A.4f})$$

$$B_7 = -\mathbf{g}vB_y - (uB_x + wB_z), \quad (\text{A.4g})$$

and

$$B_8 = -wB_y + (2 - \mathbf{g})vB_z. \quad (\text{A.4h})$$



## List of Figure Captions

Fig. 1: Definition of space-time mesh for a two-dimensional problem.

Fig. 2: Grid arrangement in space-time domain.

Fig. 3: Definition of Special SE and CE for a inherent constrained-transport scheme.

Fig. 4: Relation between  $x$ - $y$  coordinates and  $\mathbf{x}$ - $\mathbf{h}$  coordinates. Rectangle OABC is the computational domain.

Fig. 5: Solution to a shock tube, Solid lines stand for one-dimensional results by Toth [12], dots for present results.

5a. Density.

5b. Pressure.

5c. Velocity component  $U_x$ .

5d. Velocity component  $U_h$ .

5e. Magnetic field component  $B_h$ .

Fig. 6: Comparison between different CESE schemes for a MHD shock tube problem.

6a. Profiles of P

6b. Profiles of  $B_h$ .

Fig. 7: Profiles of  $B_x$  for a MHD shock tube problem from different CESE schemes.

Fig. 8: Pressure contours of a MHD vortex problem by the original CESE scheme.

8a. Pressure contours  $t = 0.5$ .

8b. Pressure contours  $t = 2$ .

8c. Pressure contours  $t = 3$ .

Fig. 9: Pressure profile of a MHD vortex problem along line  $y = 0.625\pi$ .

9a. Pressure profile at  $t = 0.5$ .

9b. Pressure profile  $t = 2$ .

9c. Pressure profile  $t = 3$ .

Fig. 10: Evolution of magnetic energy of a MHD vortex problem.

Fig. 11: Comparison between CESE method with and without a projection procedure for maintaining  $\nabla \cdot \mathbf{B} = 0$ .

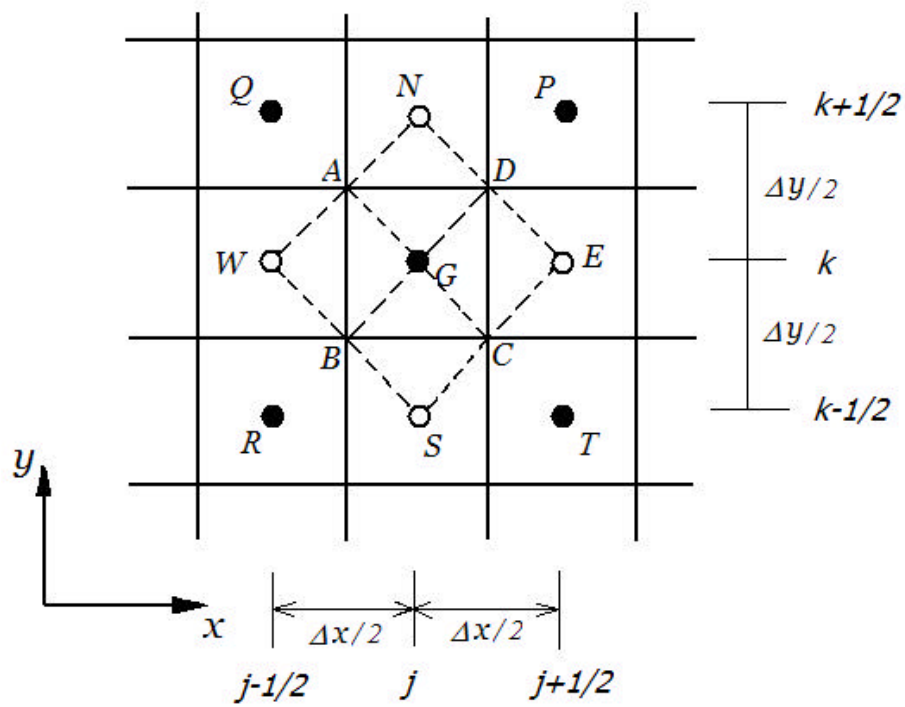


Fig. 1: Definition of space-time mesh for a two-dimensional problem.

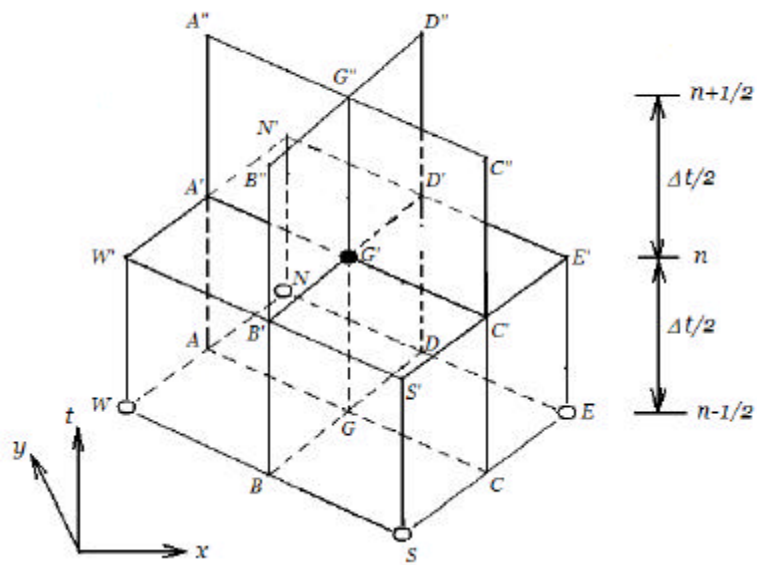


Fig. 2: Grid arrangement in space-time domain.

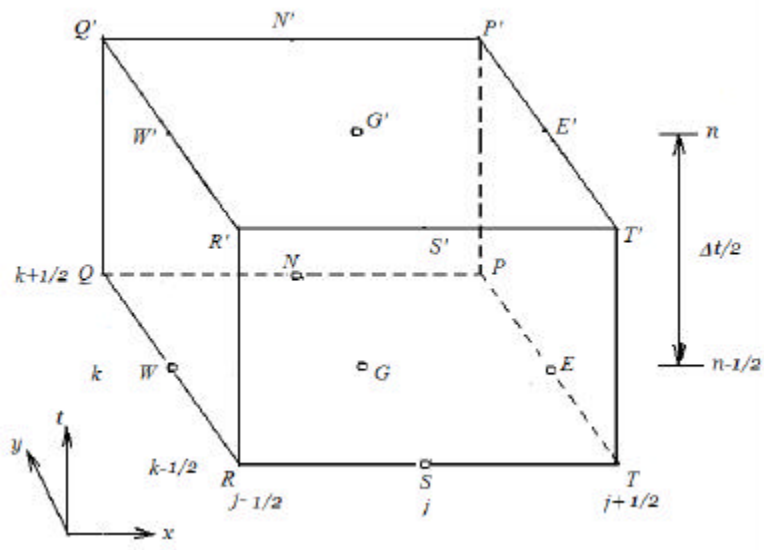


Fig. 3: Definition of Special SE and CE for a inherent constrained-transport scheme.

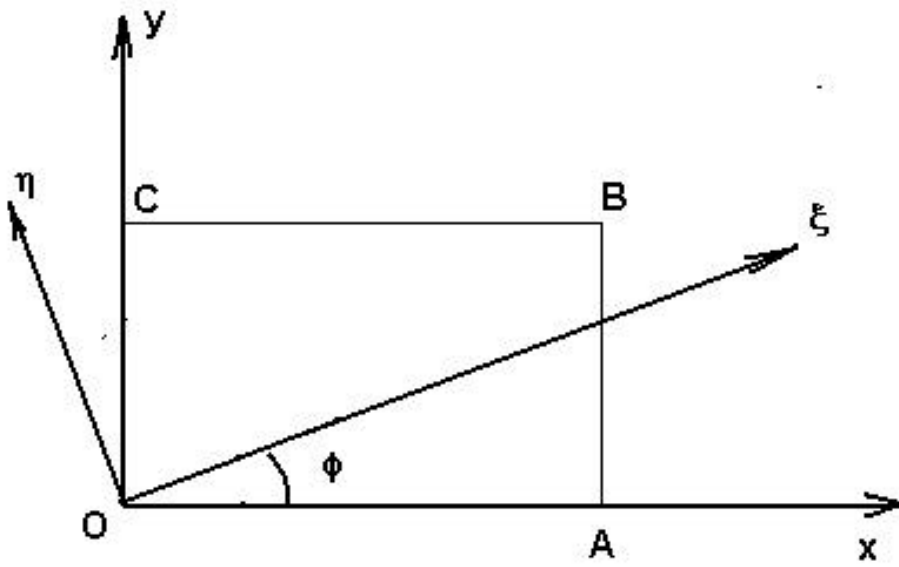
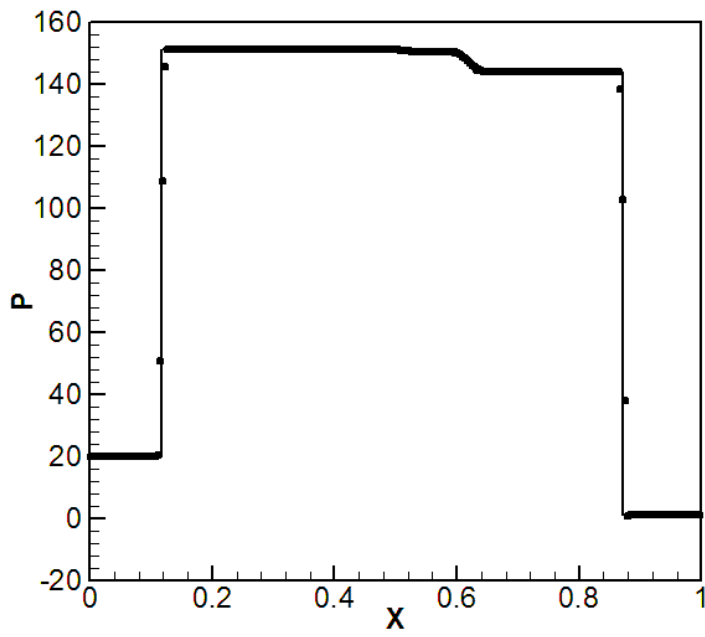
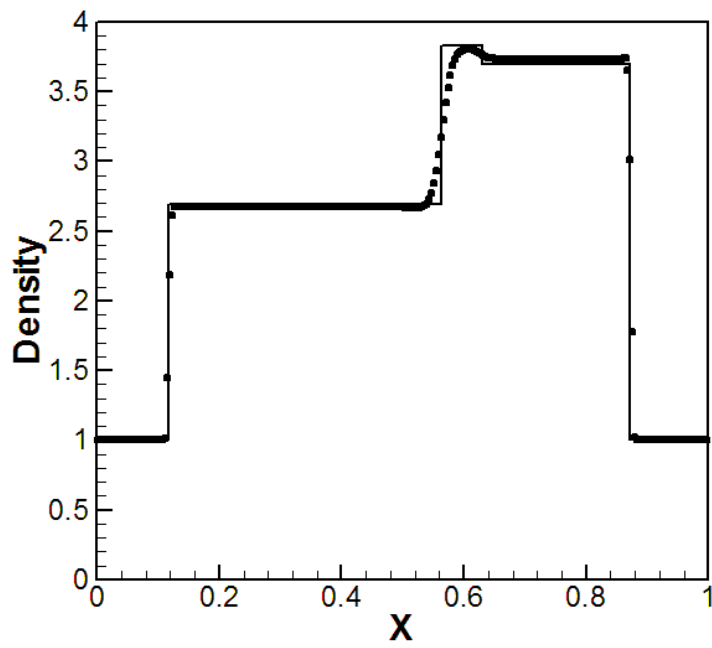


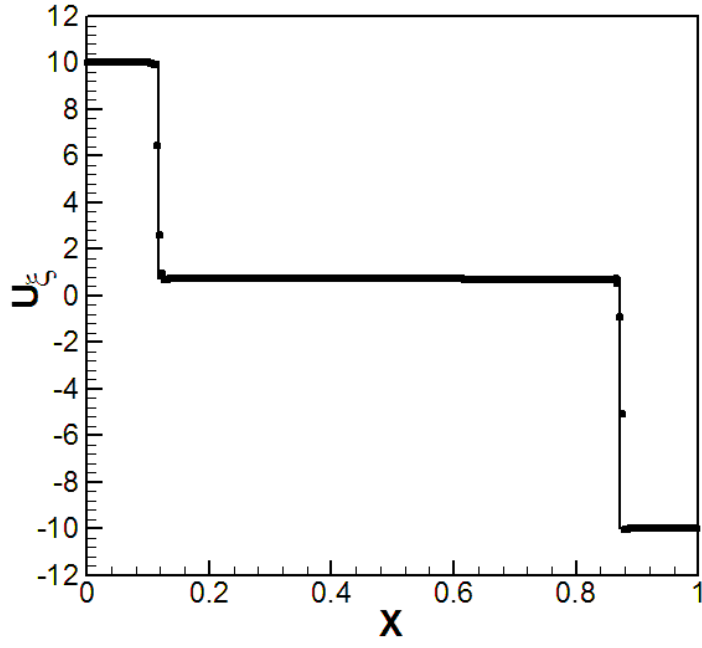
Fig. 4: Relation between  $x$ - $y$  coordinates and  $\xi$ - $\eta$  coordinates. Rectangle  $OABC$  is the computational domain.



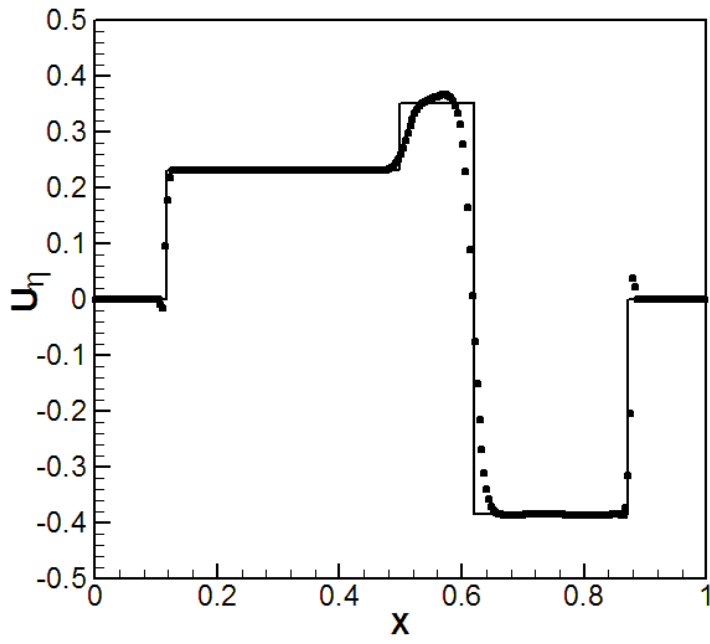
5a. Pressure.



5b. Density.

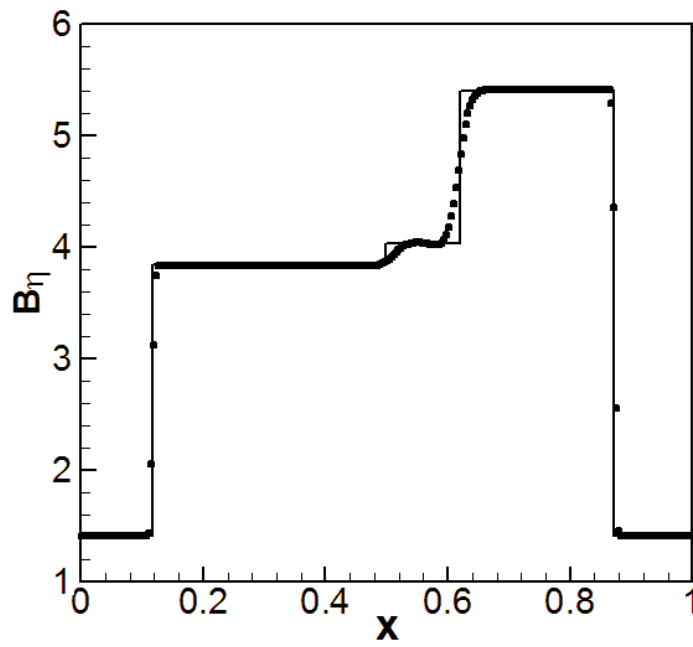


5c. Velocity component  $U_x$



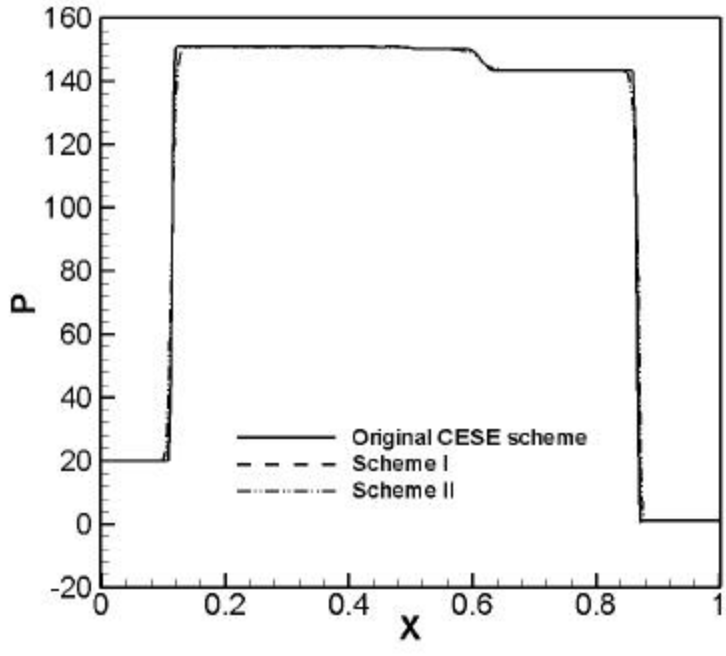
5d. Velocity component  $U_h$



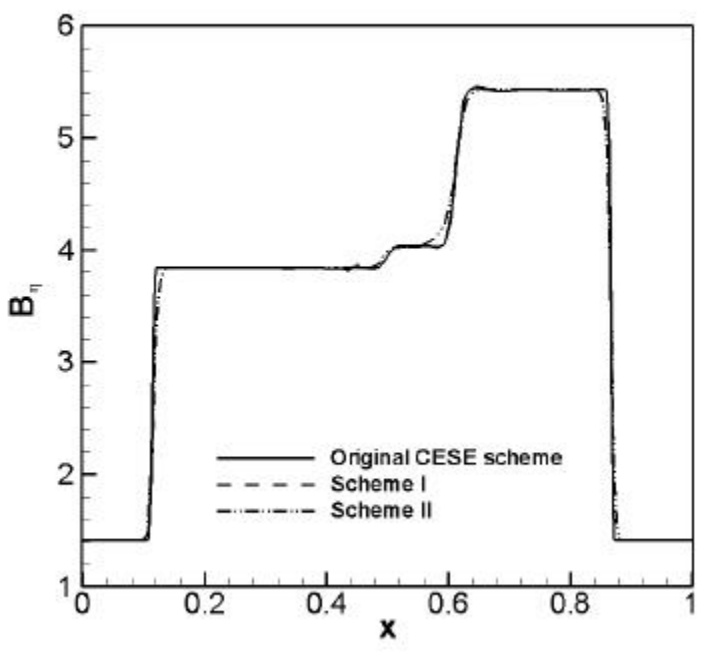


5e. Magnetic field component  $B_h$ .

Fig. 5: Solution to shock tube B. Solid lines stand for one-dimensional results by Toth [12], dots for present results.



6b. Profiles of P



6b. Profiles of  $B_\eta$

Fig. 6: Comparison between different CESE schemes for a MHD shock tube problem.

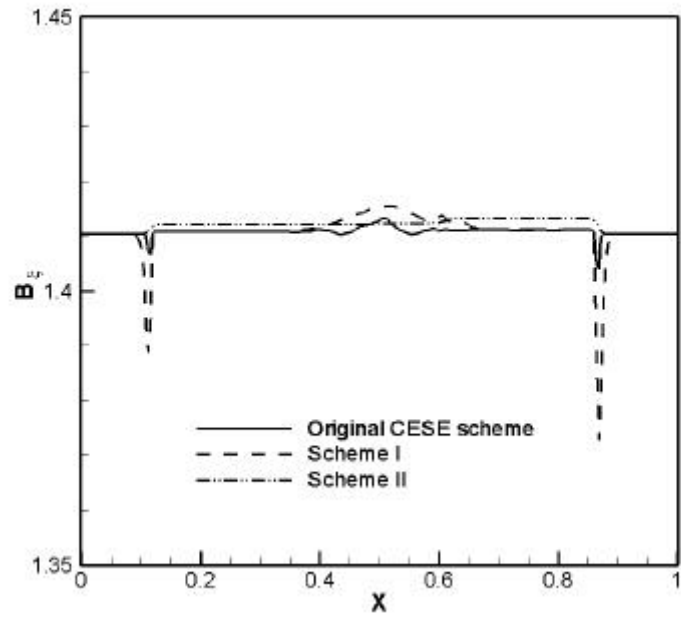
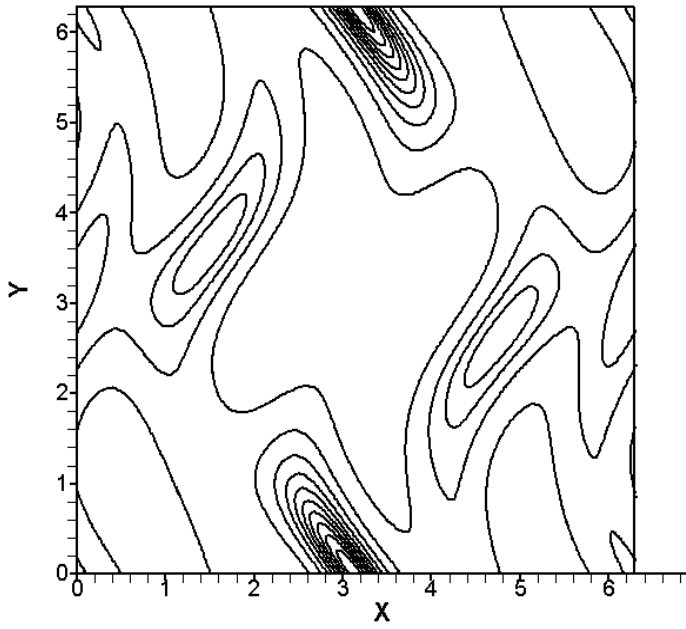
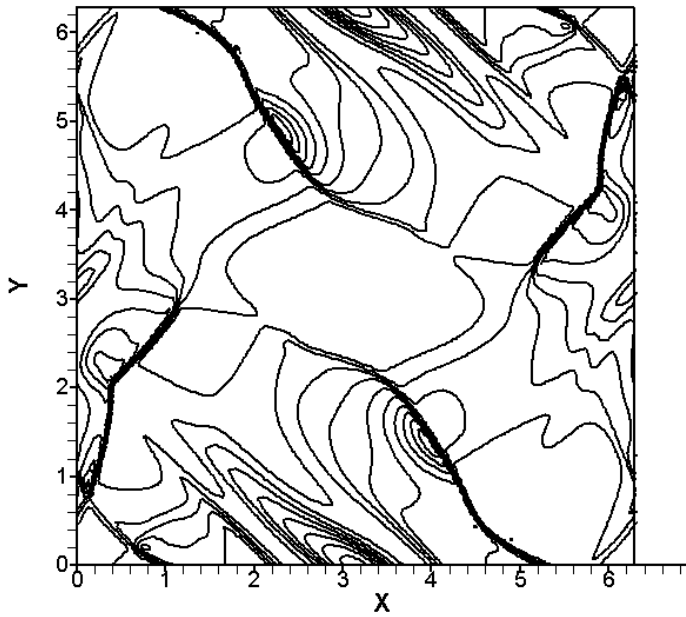


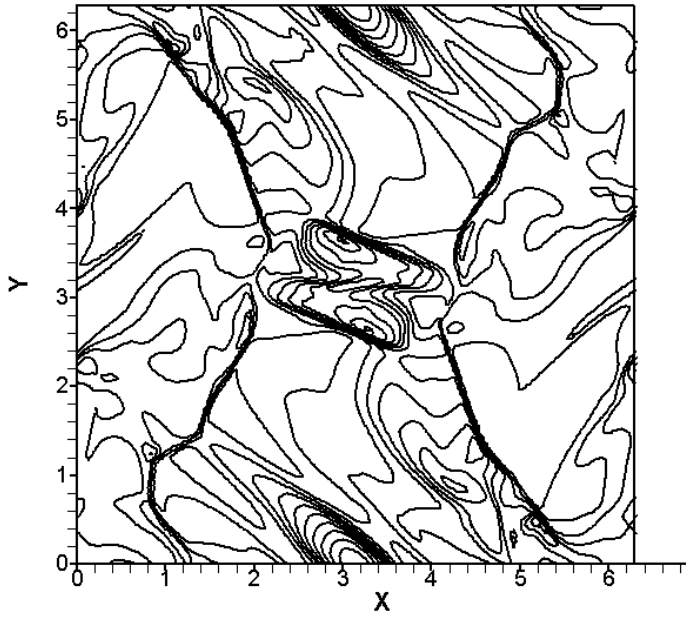
Fig. 7: Profiles of  $B_x$  for a MHD shock tube problem with different CESE schemes.



8a. Pressure contours  $t = 0.5$ .

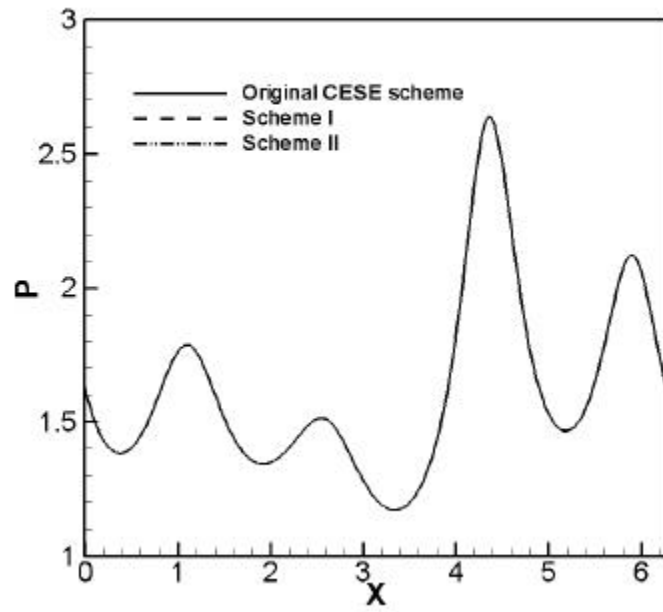


8b. Pressure contours  $t = 2$ .

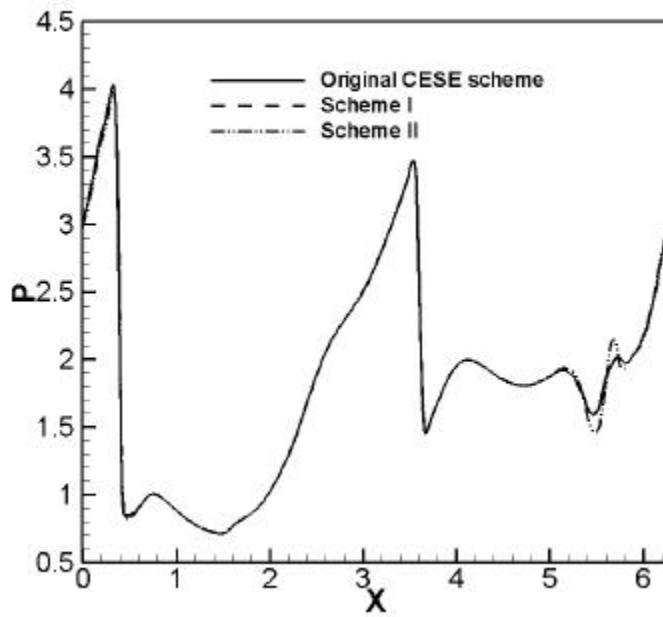


8c. Pressure contours  $t = 3$ .

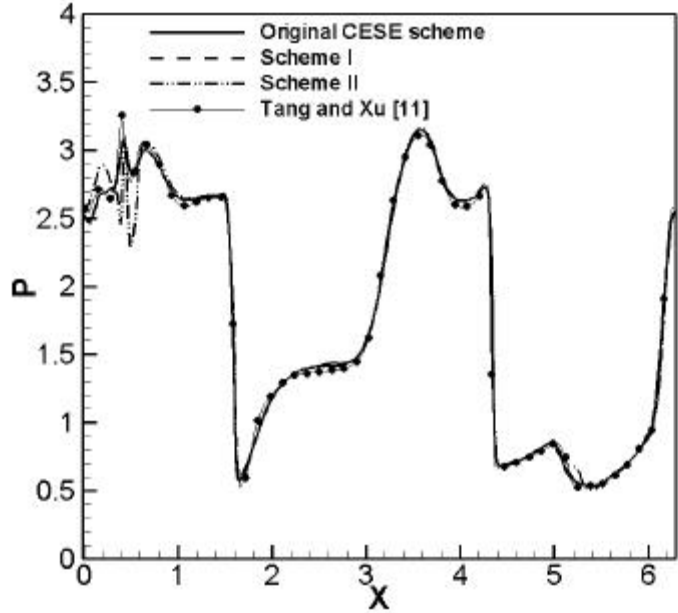
Fig.8: Pressure contours of a MHD vortex problem by the original CESE scheme.



9a. Pressure profile at  $t = 0.5$ .



9b. Pressure profile  $t = 2$ .



9c. Pressure profile  $t = 3$ .

Fig. 9: Pressure profile of a MHD vortex problem along line  $y = 0.625\pi$ .

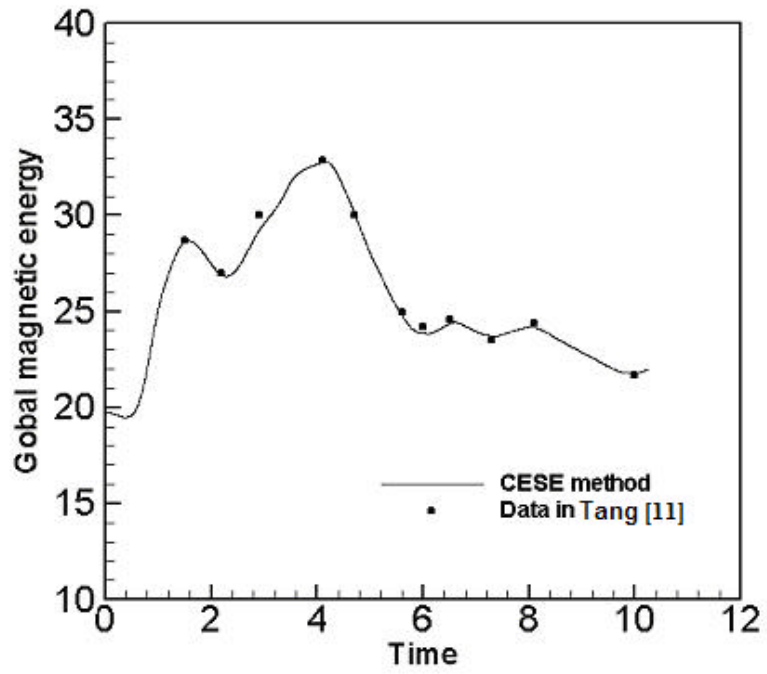


Fig. 10: Evolution of magnetic energy of a MHD vortex problem.



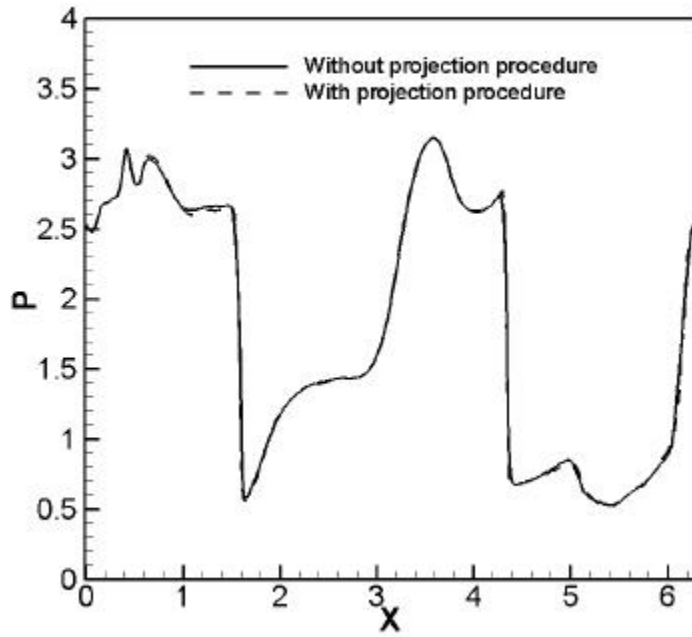


Fig. 11: Comparison between CESE method with and without a projection procedure for maintaining  $\nabla \cdot \mathbf{B} = 0$ .